Applied Water Science (2023) 13:52
https://doi.org/10.1007/s13201-022-01854-6

ORIGINAL ARTICLE

# Reactive red-141 removal from synthetic solutions by γ-$Al_2O_3$ nanoparticles: process modeling, kinetic, and isotherm studies

Ziaeddin Bonyadi[1,2] · Zeinab Fouladi[2] · Akram Robatjazi[2] · Mohaddeseh Zahmatkesh Anbarani[2]

Received: 1 June 2022 / Accepted: 12 December 2022 / Published online: 30 December 2022


## Abstract

Azo dyes can cause problems such as allergies, mutagenicity, allergies, and carcinogenesis in humans in addition to having ecological effects in aquatic environments. This study emphasizes the removal of RR-141 by γ-$Al_2O_3$ NPs from the aqueous solution. To obtain the optimum conditions of RR-141 removal using the BBD model, the main factors such as the initial RR-141 level (10–70 mg/L), pH (3–9), contact time (10–70 min), and γ-$Al_2O_3$ NPs dose (0.2–0.8 g/L) were tested. According to the quadratic model, the highest removal rate (97.74%) was found at the pH of 4.81, the contact time of 51.61 min, the γ-$Al_2O_3$ NPs dose of 0.38 g/L, and the RR-141 level of 10 mg/L. The RR-141 removal follows the pseudo-second-order and Langmuir models. The highest absorption capacity for RR-141 was 40.65 mg/g. The results of this study showed that γ-$Al_2O_3$ NPs significantly removed RR-141 from aqueous solution.

**Keywords** Adsorption · Reactive red-141 · γ-$Al_2O_3$ · Nanoparticles

## Abbreviations

| | |
|---|---|
| RR-141 | Reactive red-141 |
| NPs | Nanoparticles |
| FT-IR | Fourier transform infrared spectroscopy |
| pHzpc | Zero point of charge |
| EDX | Energy-dispersive X-ray |
| FESEM | Field emission scanning electron microscopy |
| ANOVA | Analysis of variance |
| BBD | Box–Behnken design |

## Introduction

Pollution of aquatic environments by heavy metal ions, azo dyes, and organic dyes is one of the environmental problems that causes global concern (Foroutan et al. 2020). Dyes are a category of organic compounds which are widely used in textile, paper, food, printing, plastic, beverages, leather, and pharmacology industries (Esvandi et al. 2020). Many harmful dyes are widely used in various industrial processes such as leather, printing, textiles, and plastics (Lei et al. 2017). The entry of dye pollutants into aquatic environments can cause problems for the environment (Abbas et al. 2020). Among these pollutants, azo dyes can be dangerous and even carcinogenic due to their nature and poor degradability. Therefore, stricter environmental regulations are in place to effectively remove these pollutants from aquatic environments (Mazloomi et al. 2021). Synthetic dyes adversely affect aquatic environments. For example, these pollutants reduce the penetration of light into water and thus disrupt the process of photosynthesis, which leads to a decrease in dissolved oxygen and an increase in the concentration of organic matter in the aqueous environment (Ramavandi et al. 2019). Under these conditions, the spontaneous treatment capacity of rivers, streams, and other aquatic environments decreases. Moreover, azo dyes are usually reactive, toxic, and may cause allergies, irritants, mutations, and cancer in humans (Ramavandi et al. 2014). Dyes used in various

✉ Ziaeddin Bonyadi
Bonyadiz@mums.ac.ir

✉ Mohaddeseh Zahmatkesh Anbarani
M.zahmatkesh9677@gmail.com

Zeinab Fouladi
Fouladiz961@mums.ac.ir

Akram Robatjazi
Robatjazia961@mums.ac.ir

[1] Social Determinants of Health Research Center, Mashhad University of Medical Sciences, Mashhad, Iran

[2] Department of Environmental Health Engineering, School of Health, Mashhad University of Medical Sciences, Mashhad, Iran

industries are divided into three categories of cationic (base colors), anionic (direct, acidic, and reactive), and non-ionic (dispersed) (Foroutan et al. 2021a, b). Anionic dye of RR-141 has a complex and circular structure with high molecular weight (Rodrigues et al. 2019). Most of natural adsorbents including zeolite, clay, etc., generally have the drawbacks for dye removal including high adsorption contact time, loss of resistance to acidic solutions, and problem in separating the adsorbent, which limit their applications (Hassanzadeh-Tabrizi et al. 2016).

So far, various technologies, including membrane filtration (Liu et al. 2020), photocatalysis (Chandrabose et al. 2021), coagulation–flocculation (Moghaddam et al. 2010), ion exchange (Joseph et al. 2020), biological system (Shabbir et al. 2017), *Phoenix dactylifera* (Asgari et al. 2014), bimetal chitosan (Asgari et al. 2013), acrylamide/graphene oxide-bonded sodium alginate nanocomposite (Pashaei-Fakhri et al. 2021), and zeolite/$Fe_3O_4$ nanocomposite (Afshin et al. 2020), have been used for the dye removal. Recently, adsorption-based techniques for the removal of dye contaminants have attracted much attention due to their high efficiency, low manufacturing and maintenance costs, and easy and simple operating process (Osagie et al. 2021). Nanoparticles are materials that can be easily attached to other atoms due to the fact that most of the atoms on their surface are unsaturated. Therefore, these materials have a high adsorption capacity and act quickly in pollutant removal processes (Bonyadi et al. 2022).

$Al_2O_3$ and their composites, due to their high performance, are still used to remove dyes and other organic molecules (Al-Salihi et al. 2022). These nanoparticles have unique properties such as reactive nature, stability in different environments, and having a high specific surface area (Adlnasab et al. 2019). Hafdi et al (2020) removed 96% of RR-141 dye using nickel oxide at the concentration of 20 mg/L, the pH of 6, the adsorbent dose of 0.1 g/L, the contact time of 40 min (Hafdi et al. 2020). In the study of Zhang et al. (2007), trivalent thallium was completely removed from the aqueous solution at pH 4.5 using $Al_2O_3$ nanoparticles (Zhang et al. 2008). In a study, the maximum removal of black eriochrome t using $Al_2O3$ nanoparticles was 89.21% (Abbas et al. 2020). Therefore, this work has focused on the RR-141 removal from the aqueous solutions using $Al_2O_3$ nanocomposite. The removal process of RR-141 was also tested to better understand the adsorption mechanism by isotherm and kinetic models. The purpose of this research was to determine the efficiency of $\gamma$-$Al_2O_3$ NPs in removing RR-141 from aqueous solution. The removal efficiency of RR-141 was also investigated by isotherm and kinetic studies to better understand the adsorption mechanism.

## Methods and materials

### Materials

The $\gamma$-$Al_2O_3$ NPs with 99.8% purity were obtained from the Iranian Nanomaterials Pioneers company. RR-141, hydrochloric acid, hydroxide sodium were prepared from the Merck company. Double-distilled water was used for the preparation of reaction mixture. The stoke solution was prepared at a concentration of 500 mg/L. Figure 1 indicates the structural formula of RR-141.

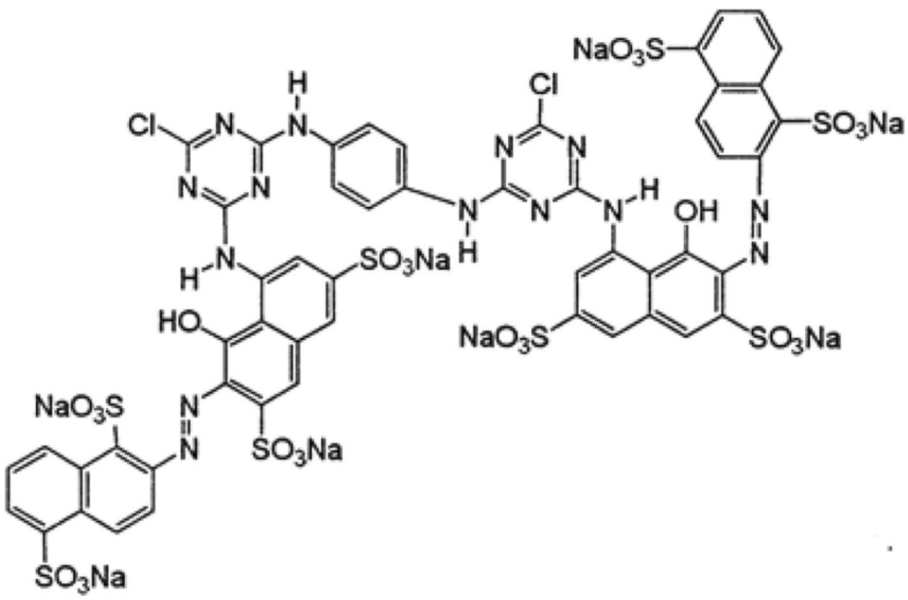


**Fig. 1** Structural formula of RR-141

## Characteristics of γ-$Al_2O_3$ NPs

The characteristics of γ-$Al_2O_3$ NPs surface was investigated by FT-IR and field emission FESEM.

The FT-IR spectrometer (Broker victor 22) was used for determining the functional groups on the γ-$Al_2O_3$ NPs surface and the interaction between the existing functional groups and RR-141 after the adsorption process. The FESEM test was utilized to investigate surface morphology of γ-$Al_2O_3$ NPs.

## Preparation of reaction mixtures

A 100 mL of reaction mixture was prepared in the presence of main factors such as initial dye concentration (10–70 mg/L), reaction time (10–70 min), γ-$Al_2O_3$ NPs dose (0.2–0.7 g/L), and pH (3–9) and then stirred using a magnetic shaker (Parsazazma model, Iran) at a fixed speed of 250 rpm. Table 1 indicates range and levels of main parameters used for the RR-141 adsorption.

At the end of the reaction time, 10 ml of the sample was taken up from the reaction mixture and centrifuged at 12,000 rpm for 12 min.

The supernatant was filtered and finally the residual RR-141 was determined by a spectrophotometer at λmax 512 nm. RR-141 removal rate was calculated from the following formula:

$$RR141\ \text{removal}\% = \frac{\left(C_0 - Ce\right) \times 100}{C_0} \tag{1}$$

where $C_0$ is the initial RR-141 concentration (mg/L); $C_e$ is the RR-141 concentration in the treated solution after a given time (mg/L).

$$q_e = \frac{(C_0 - C_e)}{m} \times V \tag{2}$$

where $W$ is the mass of γ-$Al_2O_3$ NPs (g), and $V$ is the volume of reaction mixture (L).

**Table 1** Range and levels of main parameters used for the RR-141 adsorption

| Factor | Variable level | | | |
|---|---|---|---|---|
| | Code | −1 | 0 | +1 |
| RR-141 concentration (mg/L) | A | 10 | 40 | 70 |
| γ-$Al_2O_3$ NPs (g/L) | B | 0.2 | 0.5 | 0.8 |
| pH | C | 3 | 6 | 9 |
| Contact time (min) | D | 10 | 40 | 70 |

## Modeling RR-141 removal

The BBD model was used for the optimization of RR-141 removal by γ-$Al_2O_3$ NPs. Based on BBD, the quadratic model is suggested as the following equation:

$$Y = \beta_0 + \sum_{i=1}^{k} \beta_i x_i + \sum_{i=1}^{k} \beta_{ii} x_i^2 + \sum_{1 \le i \le j}^{k} \beta_{ij} x_i x_j \tag{3}$$

where $Y$, $\beta_0$, $\beta_i$, $\beta_{ii}$, $\beta_{ij,}$ and $x_i$ or $x_j$ illustrate the predicted response, the constant coefficient, regression coefficients for linear impacts, quadratic coefficients, interaction coefficients, and the coded values of the parameters, respectively.

## Adsorption kinetic and isotherm studies

By conducting synthetic studies, the actual treatment system can be designed based on the existing conditions. For this step, a 100 ml of synthetic solution containing the RR-141 concentration of 20–160 mg/L, the pH of 7, the γ-$Al_2O_3$ NPs dose of 0.5 g/L, and the contact time of 15–90 min prepared. Kinetic models including quasi-first-order, quasi-second-order, and intraparticle diffusion were used to investigate the dye adsorption onto the NPs. In addition, Freundlich, Langmuir, and Temkin isotherms were considered for this study. The equations of kinetic and isotherm models can be deduced from the studies of Davoudi et al. (2019) and Mohebrad et al. (2019).

## Regeneration study

From an economic point of view, the efficiency of the regenerated adsorbent in removing environmental pollutants is important. In this work, initially, to select the appropriate conditions (acidic or alkaline), the regeneration of nanoparticles was carried out under acidic (pH = 4) and alkaline (pH = 12) solutions. After a series of adsorption and desorption experiments, it was found that the nanoparticles are more efficient under alkaline conditions. After performing a series of adsorption and desorption experiments, it was found that the efficiency of regenerated nanoparticles is higher in alkaline conditions than in acidic conditions. Therefore, the nanoparticles were reproduced under alkaline conditions and its effect on other major laboratory parameters was investigated.

## Results and discussion

### Characterization

#### FTIR

The presence of functional groups on adsorbent surface and their effect on RR-141 removal were analyzed by FTIR method. Figure 2 shows FTIR spectra of fresh and used $\gamma$-$Al_2O_3$ NPs. The FTIR spectrum of adsorbent before RR-141 removal indicates different main intense bands, about 538, 632, 751, 814, 1507, 1638, and 3443 $cm^{-1}$ (Fig. 2a). The peaks at 1507, 1638, and 3443 $cm^{-1}$ were correlated with the stretching vibration of the –OH group from Al–OH and bending vibration of –OH groups, respectively (Andani et al. 2020). The peaks at 538 $cm^{-1}$ and 632 $cm^{-1}$ were attributed to Al–O (El Gaayda et al. 2021).

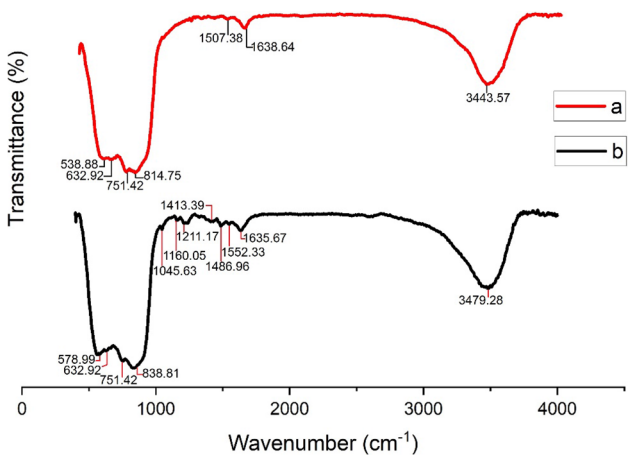


**Fig. 2** FTIR spectra of **a** before and **b** after RR-141 adsorption

In Fig. 2b, the situation of some peaks has changed after RR-141 adsorption. The change of the 3443 $cm^{-1}$ peak to 3479 $cm^{-1}$ offers the attachment of RR-141 on –OH group. Foroutan et al. (2019) obtained similar results (Foroutan et al. 2019). The change in a peak at 16,507 to 1552 $cm^{-1}$ signifies the involvement of the C=O group. Furthermore, the peak at 1073.94 $cm^{-1}$ was altered to 1045 $cm^{-1}$, indicating the involvement of a carboxylate group ($COO^-$) in the adsorption of basic RR-141 (Nath Ray 2015).

#### FESEM

Figure 3 shows the FESEM images of $\gamma$-$Al_2O_3$ NPs before and after adsorption. FESEM analysis indicated that before the adsorption process, the surface of $\gamma$-$Al_2O_3$ NPs has an irregular surface with different pores. These pores are effective in absorbing RR-141 molecules. However, after the adsorption process, the pores observed on the nanoparticle surface were blocked due to dye adsorption. Based on this, it can be stated that these of $\gamma$-$Al_2O_3$ NPs have a large and accessible surface for RR-141 adsorption (Foroutan et al. 2018).

#### $pH_{zpc}$

The $pH_{zpc}$ is an important test to identify the adsorption mechanisms. According to Fig. 3, a $pH_{zpc}$ of nanoparticles was 6.25. Therefore, the surface charge of adsorbent for pH values above or below 6.25 is negative or positive charge, respectively.

### Modeling of the RR-141 removal rate

In this research, the RR-141 removal in the presence of main parameters, including the initial RR-141 level, the dose of

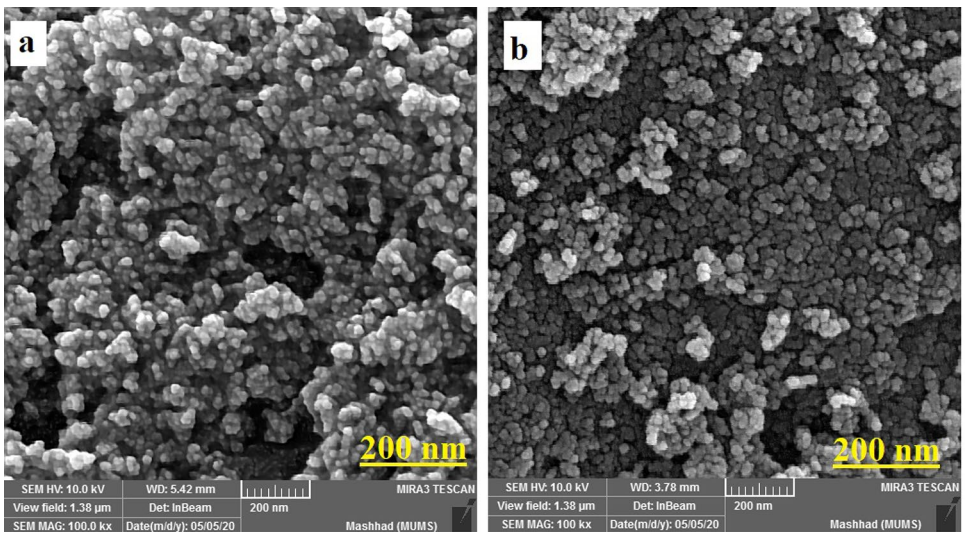


**Fig. 3** FESEM images of $\gamma$-$Al_2O_3$ NPs **a** before adsorption and **b** after adsorption

**Table 2** BBD matrix for RR-141 removal using γ-$Al_2O_3$ NPs

| Run no | Coded variable | | | | Removal (%) | Run no | Coded variable | | | | Removal (% |
|---|---|---|---|---|---|---|---|---|---|---|---|
| | A | B | C | D | | | A | B | C | D | |
| 1 | 0 | −1 | 1 | 0 | 27.72 | 16 | 0 | 1 | 1 | 0 | 54.91 |
| 2 | 1 | 0 | 1 | 0 | 28.92 | 17 | 1 | 0 | 0 | 1 | 41.46 |
| 3 | −1 | 0 | 1 | 0 | 95 | 18 | −1 | 1 | 0 | 0 | 68.92 |
| 4 | −1 | 0 | 0 | 1 | 80.83 | 19 | 0 | 0 | 0 | 0 | 83.71 |
| 5 | 0 | 1 | 0 | 1 | 50.07 | 20 | 1 | 0 | −1 | 0 | 78.57 |
| 6 | 0 | −1 | −1 | 0 | 62.09 | 21 | 0 | 0 | −1 | −1 | 69.1 |
| 7 | 0 | 0 | 1 | 1 | 52.82 | 22 | 0 | 1 | 0 | −1 | 56.37 |
| 8 | 0 | 0 | 1 | −1 | 57.23 | 23 | 1 | 0 | 0 | −1 | 43.38 |
| 9 | 0 | 0 | 0 | 0 | 72.87 | 24 | 0 | −1 | 0 | 1 | 58.16 |
| 10 | −1 | 0 | −1 | 0 | 98.34 | 25 | 0 | 1 | −1 | 0 | 62.3 |
| 11 | 0 | −1 | 0 | −1 | 37.52 | 26 | 1 | 1 | 0 | 0 | 59.27 |
| 12 | 0 | 0 | 0 | 0 | 80.17 | 27 | −1 | 0 | 0 | −1 | 67.55 |
| 13 | 0 | 0 | −1 | 1 | 76.23 | | | | | | |
| 14 | −1 | −1 | 0 | 0 | 87.66 | | | | | | |
| 15 | 1 | −1 | 0 | 0 | 20.88 | | | | | | |

**Table 3** Statistical adequacy evaluation of models

| Source | Sequential *p* value | Lack of fit *p* value | Adjusted $R^2$ | Predicted $R^2$ |
|---|---|---|---|---|
| Linear | 0.0008 | 0.1245 | 0.4857 | 0.3572 |
| 2FI | 0.1830 | 0.1422 | 0.5691 | 0.3095 |
| Quadratic | 0.0002 | 0.4806 | 0.8986 | 0.7505 |
| Cubic | 0.9641 | 0.1787 | 0.7909 | −2.8176 |

$\gamma$-$Al_2O_3$ NPs, contact time, and pH the removal rate, was studied. The data of RR-141 removal using $\gamma$-$Al_2O_3$ NPs are shown in Table 2.

From Table 2, the highest and lowest removal rates were 98.34 and 20.88, respectively. Table 3 shows the statistical adequacy evaluation of models. The experimental results were statistically evaluated for linear, 2Fl, quadratic, and cubic models to choose the model that best explains the data. Figure 4 indicates the impact of pH on zeta potential of the $\gamma$-$Al_2O_3$ NPs.

According to Table 3, the quadratic model was suggested to fit the obtained findings. Table 4 offers comparative model regression findings. Table 4 estimates the coefficients for the quadratic model of RR-141 removal by $\gamma$-$Al_2O_3$ NPs.

According to Table 4, the quadratic model for dye removal (R) in terms of coded parameters is expressed as Eq. 4:

$$\begin{aligned} R = {} & 78.92 - 18.82A + 4.82B - 10.84C + 2.37D \\ & + 14.28AB - 11.58AC - 3.80AD + 6.74BC \\ & - 6.73BD - 2.89CD - 2.92A^2 - 18.53B^2 \\ & - 3.86C^2 - 12.92D^2 \end{aligned} \quad (4)$$

As can be seen from Eq. 4, each model has two fixed and variable parts. From Eq. 4, the dye removal efficiency was

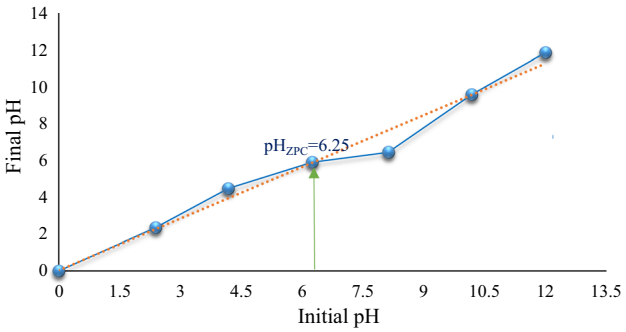


**Fig. 4** The impact of pH on zeta potential of the $\gamma$-$Al_2O_3$ NPs

78.92%. The main parameters coded as A, B, C, D with coefficients of − 18.82, + 4.82, − 10.84 and + 2.37, respectively, affected the removal efficiency of RR-141. A code with a coefficient of − 18.82 had the greatest effect on the removal of RR-141. In addition, AB and B2 codes had the most interaction and square effects on dye removal, respectively.

Table 5 illustrates ANOVA for quadratic model of R141 removal using $\gamma$-$Al_2O_3$ NPs. Overall, the findings of Table 5 indicated that the RR-141 removal rate was statistically significant (P-value < 0.05). Also, the values of $R^2$, adjusted $R^2$, predicted $R^2$, and adequacy precision were found to be 0.95,

**Table 4** Coefficients estimation for quadratic model of RR-141 removal

| Factor | Coefficient estimate | df | Standard error | 95%CI low | 95%CI high | VIF |
|---|---|---|---|---|---|---|
| Intercept | 78.92 | 1 | 3.72 | 70.82 | 87.02 | |
| A-time | − 18.82 | 1 | 1.86 | − 22.87 | − 14.77 | 1 |
| B-conc | 4.82 | 1 | 1.86 | 0.7668 | 8.87 | 1 |
| C-pH | − 10.84 | 1 | 1.86 | − 14.89 | − 6.79 | 1 |
| D-dose | 2.37 | 1 | 1.86 | − 1.68 | 6.42 | 1 |
| AB | 14.28 | 1 | 3.22 | 7.27 | 21.30 | 1 |
| AC | − 11.58 | 1 | 3.22 | − 18.59 | − 4.56 | 1 |
| AD | − 3.80 | 1 | 3.22 | − 10.82 | 3.22 | 1 |
| BC | 6.74 | 1 | 3.22 | − 0.2710 | 13.76 | 1 |
| BD | − 6.73 | 1 | 3.22 | − 13.75 | 0.2810 | 1 |
| CD | − 2.89 | 1 | 3.22 | − 9.90 | 4.13 | 1 |
| $A^2$ | − 2.92 | 1 | 2.79 | − 8.99 | 3.16 | 1.25 |
| $B^2$ | − 18.53 | 1 | 2.79 | − 24.60 | − 12.45 | 1.25 |
| $C^2$ | − 3.86 | 1 | 2.79 | − 9.93 | 2.22 | 1.25 |
| $D^2$ | − 12.92 | 1 | 2.79 | − 19.00 | − 6.85 | 1.25 |

**Table 5** ANOVA for quadratic model of R141 removal using $\gamma$-$Al_2O_3$ NPs

| Sum of squares | | df | Mean square | *F* value | *p* value |
|---|---|---|---|---|---|
| Model | 10,132.28 | 14 | 723.73 | 17.45 | < 0.0001 |
| A-time | 4249.56 | 1 | 4249.56 | 102.46 | < 0.0001 |
| B-conc | 278.50 | 1 | 278.50 | 6.71 | 0.0236 |
| C-pH | 1408.98 | 1 | 1408.98 | 33.97 | < 0.0001 |
| D-dose | 67.31 | 1 | 67.31 | 1.62 | 0.2268 |
| AB | 815.96 | 1 | 815.96 | 19.67 | 0.0008 |
| AC | 536.15 | 1 | 536.15 | 12.93 | 0.0037 |
| AD | 57.76 | 1 | 57.76 | 1.39 | 0.2608 |
| BC | 181.98 | 1 | 181.98 | 4.39 | 0.0581 |
| BD | 181.44 | 1 | 181.44 | 4.37 | 0.0584 |
| CD | 33.29 | 1 | 33.29 | 0.8027 | 0.3879 |
| $A^2$ | 45.32 | 1 | 45.32 | 1.09 | 0.3165 |
| $B^2$ | 1831.01 | 1 | 1831.01 | 44.15 | < 0.0001 |
| $C^2$ | 79.41 | 1 | 79.41 | 1.91 | 0.1916 |
| $D^2$ | 890.62 | 1 | 890.62 | 21.47 | 0.0006 |
| Residual | 497.71 | 12 | 41.48 | | |
| Lack of fit | 436.60 | 10 | 43.66 | 1.43 | 0.4806 |
| Pure error | 61.11 | 2 | 30.55 | | |
| Cor total | 10,629.98 | 26 | | | |
| $R^2$ | 0.95 | | Predicted $R^2$ | 0.75 | |
| Adjusted $R^2$ | 0.89 | | Adeq precision | 15.03 | |

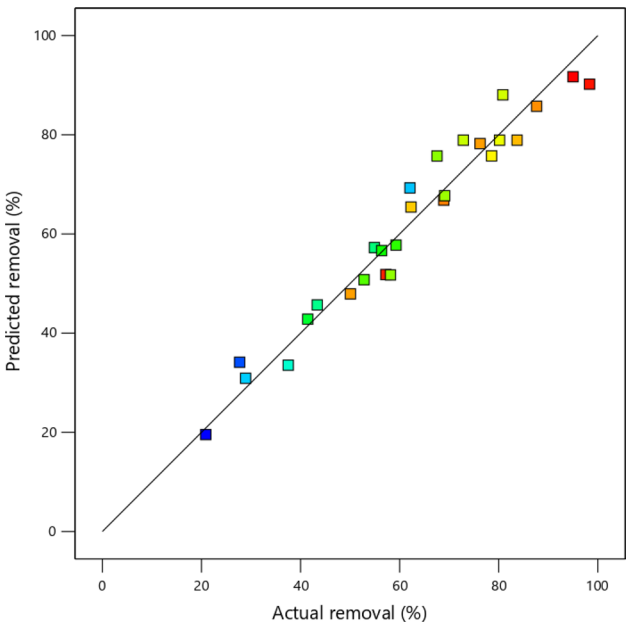


**Fig. 5** Distribution of experimental versus predicted removal for RR-141 adsorption onto $\gamma$-$Al_2O_3$ NPs

0.89, 0.75, and 15.03, respectively. Conduction of similar experiments at specified optimum conditions reveals the high repeat ability of method for prediction of real removal percentage with relative deviation less than 2%.

Figure 5 indicates the rate of actual removal versus the rate of predicted removal. From Fig. 5, the adequacy of the model to provide a good prediction for the efficiency of RR-141 removal is obvious.

## The effect of main factors on removal efficiency

Figure 6a–b displays the impact of initial RR-141 level, $\gamma$-$Al_2O_3$ dose, pH, and contact time on the efficiency of RR-141 removal

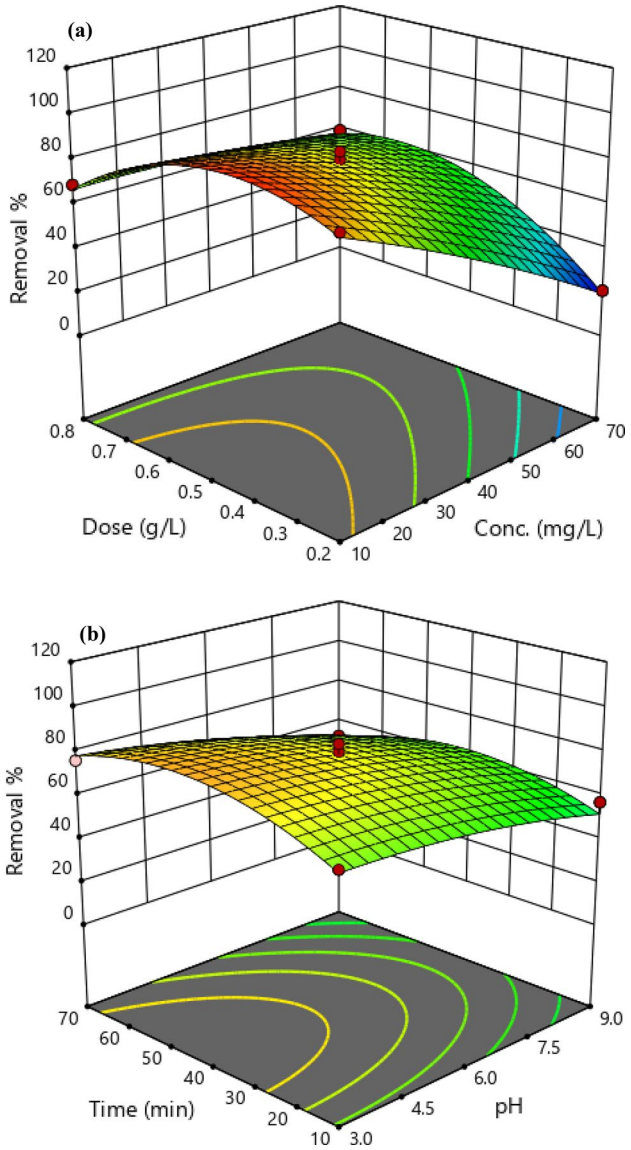


**Fig. 6** Response surface plot about the effects of **a** dose versus Conc. RR-141, **b** pH versus time

## Initial dye concentration and its effect

The findings of Fig. 6a show that with increasing dye concentration, the removal efficiency decreases ($P$ value < 0.05). The highest (94%) and lowest (57%) removal efficiencies were obtained at concentrations of 10 mg/L and 70 mg/L, respectively. The reducing trend of removal rate with enhancing level may be due to the existence of high unoccupied sites on the adsorbent surface to absorb dye at low dye levels, while the saturation of active binding sites with dye molecules at higher levels reduced the RR-141 removal rate (Wu et al. 2016; Navaeia et al. 2019). The higher removal efficiency of nano-$SiO_2$-$Al_2O_3$ at low initial concentration of methyl orange could be related to the high proportion of initial mole numbers of methyl orange to the available active places on the surface area; hence, the fractional adsorption is related to the initial concentration (Arshadi et al. 2013).

## Effect of adsorbent dose

The findings of Fig. 6a indicated that dye removal was directly related to the dose of $\gamma$-$Al_2O_3$ NPs, so that by increasing the dose of $\gamma$-$Al_2O_3$ NPs from 0.2 to 0.8 g/L, the removal rate of RR-141 enhanced from 55 to 65%. As the adsorbent dose increases, the number of active and hollow sites increases, resulting in the adsorption of more dye molecules, which leads to an increase in removal efficiency (Foroutan et al. 2021a, b; Nasoudari et al. 2021; Foroutan et al. 2022).

## Contact time and its effect

According to Fig. 6a, with increasing time from 10 to 70 min, the dye removal efficiency was increased by 7% ($P$ value < 0.05). The results showed that the dye removal in the early times was faster due to the availability of a large number of free surface active sites for dye adsorption and then the removal process was balanced due to the saturation of the adsorption sites (Kataria and Garg 2019).

## pH effect

Figure 1 shows the interface level diagram of the interactions between pH and time. The findings of Fig. 6b show that with increasing the pH from 3 to 9, the color removal also decreased from 85 to 64%, respectively. The adsorption capacity was decreased with increasing pH. At alkaline pH, the dominant charge on the alumina surface is negative, leading to the excretion of anionic dye molecules. In an acidic environment, the positive charge of the adsorbent surface has a stronger affinity for anionic dyes. Under these conditions, the adsorbent surface charge becomes positive due to the protonation of Al–OH and forms Al–$OH_2^+$ groups, which leads to the adsorption of anionic dye molecules. This behavior is consistent with the zero charge point, where for pH less than 6.25 the adsorbent surface is mostly positive and adsorbs negative dye molecules (Ibrahim 2019; Fernandes et al. 2021).

## Optimum operational conditions

In this study, the results were analyzed using the BBD to obtain the highest dye removal rate. According to the quadratic model, the highest removal rate (97.74%) was found at the pH of 4.81, the contact time of 51.61 min, the $\gamma$-$Al_2O_3$ NPs dose of 0.38 g/L, and the RR-141 level of 10 mg/L.

**Table 6** The kinetic and isotherm parameters fitted for RR-141 removal using $\gamma$-$Al_2O_3$ NPs

| Kinetic model | Linear form | Parameter | Value | | | |
|---|---|---|---|---|---|---|
| | | | 20 mg/L | 40 mg/L | 80 mg/L | 160 mg/L |
| Pseudo-first order | $\log(q_e - q_t) = \log q_e - \frac{k_1}{2.303}.t$ | $q_{e,cal}$ [mg/g] | 0.30 | 0.97 | 0.92 | 0.96 |
| | | $K_1$ [$min^{-1}$] | 0.58 | 1.26 | 2.02 | 1.57 |
| | | $R^2$ | 0.77 | 0.96 | 0.99 | 0.99 |
| Pseudo-second order | $\frac{t}{q_t} = \frac{1}{k_2 qe^2} + \frac{1}{qe}.t$ | $q_{e,cal}$ [mg/g] | 5.48 | 10.74 | 11.19 | 9.87 |
| | | $K_2$ [$min^{-1}$] | −0.13 | 0.01 | 0.02 | 0.02 |
| | | $R^2$ | 0.99 | 0.99 | 0.99 | 0.99 |
| Intra-particle diffusion | $qt = k_p.t^{0.5} + c$ | $K_p$ [mg/g. $min^{-0.5}$] | 0.07 | 0.45 | 0.54 | 0.72 |
| | | $R^2$ | 0.95 | 0.97 | 0.88 | 0.98 |

| Isotherm model | Linear form | Parameter | Value |
|---|---|---|---|
| Langmuir | $\frac{Ce}{qe} = \frac{1}{qm}Ce + \frac{1}{qmb}$ | $q_{max}$ (mg/g) | 40.65 |
| | | $K_L$ (L/mg) | 0.05 |
| | | $R^2$ | 0.99 |
| Freundlich | $Log\, q_e = \log K_F + \frac{1}{n}\log Ce$ | $K_F$ mg/g(L/mg)$^{1/n}$ | 2.60 |
| | | $N$ | 1.43 |
| | | $R^2$ | 0.97 |
| Temkin | $q_e = B_1 \ln .k_t + B_1 \ln C_e$ | $k_t$ (L/mg) | 26.46 |
| | | $B_1$ | 8.16 |
| | | $R^2$ | 0.98 |

## Isotherm and kinetic models

The adsorption kinetics provide the necessary information for the modeling and design of the process, including the adsorption mechanism and the speed limiting steps (Mohammed and Kareem 2019). The experimental kinetic data were fitted in pseudo-first-order, pseudo-second-order, and intra-particle diffusion models. The kinetic and isotherm parameters fitted for RR-141 removal by $\gamma$-$Al_2O_3$ NPs are listed in Table 6. From Table 6, $R^2$ for pseudo-first-order, pseudo-second-order, and intraparticle diffusion kinetics were 0.96, 0.99, and 0.98. The value of pseudo-second-order regression coefficient ($R^2 = 0.99$) is higher than that of other models. Hence, pseudo-second-order model is best suited for RR-141. Adsorption isotherms are an important part of adsorption studies that describe the mechanisms of interaction between adsorbent and adsorption can provide useful information for a better understanding of the economics of the adsorption system (Foroutan et al. 2017; Al-Ghouti and Da'ana 2020). The sorption models also broaden our understanding of the economy of the sorption system. For this purpose, experimental equilibrium data were analyzed using

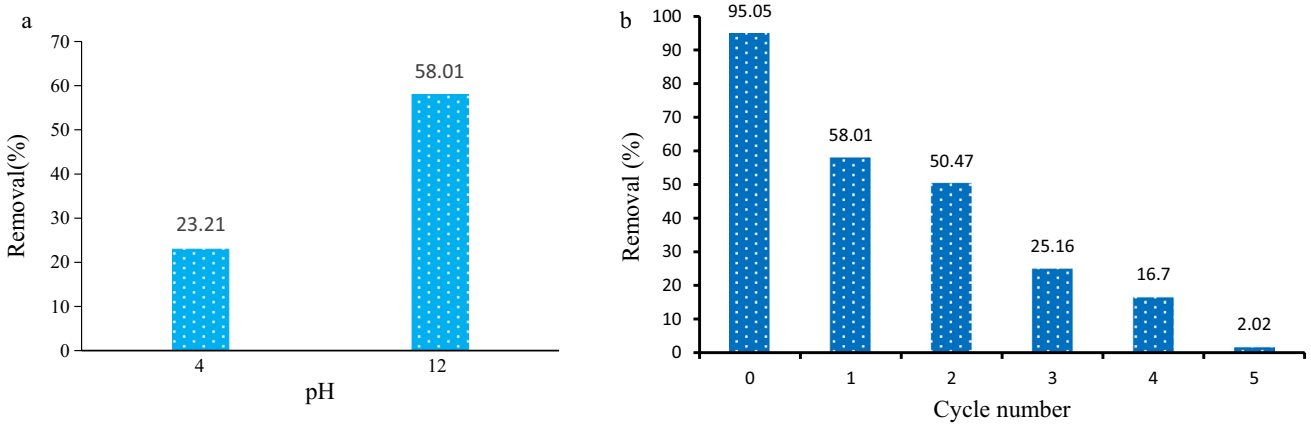


**Fig. 7** $\gamma$-$Al_2O_3$ NPs reusability; RR-141 removal efficiency for NPs regenerated by alkaline/acid eluting solution (**a**) and RR-141 removal in consecutive adsorption/desorption cycles (**b**)

**Table 7** Comparison of Langmuir adsorption capacities of RR-141 with results from previous studies

| Adsorbent | Adsorbate | Reference |
|---|---|---|
| RR-141 [mg.g$^{-1}$] | | |
| *Carica papaya* wood | 52.63 | (Rangabhashiyam et al. 2018) |
| Alginate/$Al_2O_3$ | 48 | (Mohammadi et al. 2014) |
| Rubber wood sawdust | 36.50 | (Kumar and Sivanesan 2007) |
| $Al_2O_3$@ATPA@AMPA | 414.63 | (Melhi et al. 2022) |
| *Annona squamosa* seed | 25.91 | (Santhi et al. 2016) |
| Banana pseudo-stem fiber | 26.50 | (Neha et al. 2011) |
| $\gamma$-$Al_2O_3$ NPs | 40.65 | Current study |

isothermal models such as Langmuir, Freundlich, and Temkin. From Table 6, the equilibrium data are in good agreement with the Langmuir model. The higher determination coefficient for the Langmuir model presents the locations of monolayer adsorption and homogeneous adsorption at the $\gamma$-$Al_2O_3$ NPs surface. As shown, the maximum Langmuir adsorption capacity of perovskite lanthanum aluminate nanoparticles for removal of blue dye was acquired good grade (Manjunatha et al. 2019). (Veloso et al. 2020). According to the Langmuir model, the maximum adsorption capacity of $\gamma$-$Al_2O_3$ NPs was acquired to be 40.65 mg.g$^{-1}$.The same results are reported about adsorption of anionic dye by aluminum oxide; according to the Langmuir model, the maximum adsorption capacity was acquired to be 57.80 mg/g at 298 k° (El Gaayda et al. 2021).

The adsorption capacities of RR-141 with other reported adsorbents are listed in Table 7. This data propose that the $\gamma$-$Al_2O_3$ NPs have potential to remove RR-141 from aquatic solutions.

## Reusability of the $\gamma$-$Al_2O_3$ NPs

The reusability of nanoparticles is important from an environmental and economic point of view. To test the reusability of the nanoparticles, a preliminary experiment was performed to determine whether alkaline aqueous (pH 12) or acidic (pH 4) salts performed better in the separation of RR-141 molecules from the nanoparticles used. The findings of Fig. 7a showed that the removal rate of RR-141 was better for alkaline solution-regenerated nanoparticles than for acidic solution. According to Fig. 7b, the removal rate of RR-141 from the first cycle to cycle 2 decreased by about 8% and then decreased sharply in subsequent cycles. This indicates that these nanoparticles can only successfully remove RR-141 up to twice after use. The decrease in removal may be due to the blockage of active adsorption sites, strong/chemical interactions in nature, that changed surface heterogeneity (Bonyadi et al. 2021).

## Conclusion

RR-141 is an anionic color with a complex and circular structure. The removal optimization of RR-141 by $\gamma$-$Al_2O_3$ NPs was performed using the BBD model. According to the quadratic model, the highest removal rate (97.74%) was found at the pH of 4.81, the contact time of 51.61 min, the $\gamma$-$Al_2O_3$ NPs dose of 0.38 g /L, and the RR-141 level of 10 mg/L. The RR-141 removal follows the pseudo-second-order model and the Langmuir model. The highest absorption capacity for RR-141 was 40.65 mg/g. The results of this study showed that $\gamma$-Al2O3 NPs significantly removed RR-141 from aqueous solution.

**Acknowledgements** Not applicable.

**Authors' contribution** ZB wrote and edited the paper and conceived and designed the experiments; ZF performed the experiments; AR performed the experiments; MZA wrote the paper.

**Funding** The authors would like to thank the financial support provided by the Mashhad University of Medical Science (Iran) through the grant number of 970245.

**Data availability** All necessary data are included in the document.

## Declarations

**Conflict of interest** The authors declare that they have no conflict of interests.

**Ethical approval** This article does not contain any studies with human participants or animals performed by any of the authors.



## References

Abbas RF, Hami HK, Mahdi NI, Waheb AA (2020) Removal of Eriochrome Black T dye by using $Al_2O_3$ nanoparticles: central composite design, isotherm and error analysis. Iran J Sci Technol Trans A Sci 44(4):993–1000

Adlnasab L, Shekari N, Maghsodi A (2019) Optimization of arsenic removal with $Fe_3O_4$@ $Al_2O_3$@ Zn-Fe LDH as a new magnetic nano adsorbent using Box-Behnken design. J Environ Chem Eng 7(2):102974

Afshin S, Rashtbari Y, Vosoughi M, Rehman R, Ramavandi B, Behzad A, Mitu L (2020) Removal of basic blue-41 dye from water by stabilized magnetic iron nanoparticles on clinoptilolite zeolite. Rev Chem 71(2):218–229

Al-Ghouti MA, Da'ana DA (2020) Guidelines for the use and interpretation of adsorption isotherm models: a review. J Hazard Master 393:122383

Al-Salihi S, Jasim AM, Fidalgo MM, Xing Y (2022) Removal of Congo red dyes from aqueous solutions by porous $\gamma$-alumina nanoshells. Chemosphere 286:131769

Andani A, Tabatabaie T, Farhadi S, Ramavandi B (2020) MIL-101(Cr)–cobalt ferrite magnetic nanocomposite: synthesis, characterization and applications for the sonocatalytic degradation of organic dye pollutants. RSC Adv 10:32845–32855

Arshadi M, Vahid FS, Salvacion J, Soleymanzadeh M (2013) A practical organometallic decorated nano-size $SiO_2$–$Al_2O_3$ mixed-oxides for methyl orange removal from aqueous solution. Appl Surf Sci 280:726–736

Asgari G, Ramavandi B, Sahebi S (2014) Removal of a cationic dye from wastewater during purification by *Phoenix dactylifera*. Desalin Water Treat 52(37–39):7354–7365

Asgari G, Ramavandi B, Farjadfard S (2013) Abatement of azo dye from wastewater using bimetal-chitosan. Sci World J. 2013

Bonyadi Z, Noghani F, Dehghan A, van der Hoek JP, Giannakoudakis DA, Ghadiri SK, Anastopoulos I, Sarkhosh M, Colmenares JC, Shams M (2021) Biomass-derived porous aminated graphitic nanosheets for removal of the pharmaceutical metronidazole: optimization of physicochemical features and exploration of process mechanisms. Colloids Surf a: Physicochem Eng Asp 611:125791

Bonyadi Z, Khatibi FS, Alipour F (2022) Ultrasonic-assisted synthesis of $Fe_3O_4$ nanoparticles-loaded sawdust carbon for malachite green removal from aquatic solutions. Appl Water Sci 12(9):1–11

Chandrabose G, Dey A, Gaur SS, Pitchaimuthu S, Jagadeesan H, Braithwaite NSJ, Selvaraj V, Kumar V, Krishnamurthy S (2021) Removal and degradation of mixed dye pollutants by integrated adsorption-photocatalysis technique using 2-D $MoS_2$/$TiO_2$ nanocomposite. Chemosphere 279:130467

Davodi M, Alidadi H, Ramezani A, Jamali-Behnam F, Bonyadi Z (2019) Study of the removal efficiency of arsenic from aqueous solutions using *Melia azedarach* sawdust modified with FeO: isotherm and kinetic studies. Desalin Water Treat 137:292–299

El Gaayda J, Akbour RA, Titchou FE, Afanga H, Zazou H, Swanson C, Hamdani M (2021) Uptake of an anionic dye from aqueous solution by aluminum oxide particles: equilibrium, kinetic, and thermodynamic studies. Groundw Sustain Dev 12:100540

Esvandi Z, Foroutan R, Peighambardoust SJ, Akbari A, Ramavandi B (2020) Uptake of anionic and cationic dyes from water using natural clay and clay/starch/$MnFe_2O_4$ magnetic nanocomposite. Surf Interfaces 21:100754

Fernandes EP, Silva TS, Carvalho CM, Selvasembian R, Chaukura N, Oliveira LM, Meneghetti SMP, Meili L (2021) Efficient adsorption of dyes by $\gamma$-alumina synthesized from aluminum wastes: Kinetics, isotherms, thermodynamics and toxicity assessment. J Environ Chem Eng 9(5):106198

Foroutan R, Shakerian Khoo F, Ramavandi B, Abbasi S (2017) Heavy metals removal from synthetic and shipyard wastewater using *Phoenix dactylifera* activated carbon. Desalin Water Treat 82:146–156

Foroutan R, Mohammadi R, Ramavandi B, Bastanian M (2018) Removal characteristics of chromium by activated carbon/$CoFe_2O_4$ magnetic composite and *Phoenix dactylifera* stone carbon. Korean J Chem Eng 35(11):2207–2219

Foroutan R, Mohammadi R, Razeghi J, Ramavandi B (2019) Performance of algal activated carbon/$Fe_3O_4$ magnetic composite for cationic dyes removal from aqueous solutions. Algal Res 40:101509

Foroutan R, Mohammadi R, Sohrabi N, Sahebi S, Farjadfard S, Esvandi Z, Ramavandi B (2020) Calcined alluvium of agricultural streams as a recyclable and cleaning tool for cationic dye removal from aqueous media. Environ Technol Innov 17:100530

Foroutan R, Peighambardoust SJ, Esvandi Z, Khatooni H, Ramavandi B (2021a) Evaluation of two cationic dyes removal from aqueous environments using CNT/MgO/$CuFe_2O_4$ magnetic composite powder: a comparative study. J Environ Chem Eng 9(2):104752

Foroutan R, Peighambardoust SJ, Hemmati S, Khatooni H, Ramavandi B (2021b) Preparation of clinoptilolite/starch/$CoFe_2O_4$ magnetic nanocomposite powder and its elimination properties for cationic dyes from water and wastewater. Int J Biol Macromol 189:432–442

Foroutan R, Peighambardoust SJ, Boffito D, Ramavandi B (2022) Sono-photocatalytic activity of cloisite 30B/ZnO/$Ag_2O$ nanocomposite for the simultaneous degradation of crystal violet and methylene blue dyes in aqueous media. Nanomaterials 12:3103

Hafdi H, Joudi M, Mouldar J, Hatimi B, Nasrellah H, El Mhammedi M, Bakasse M (2020) Design of a new low cost natural phosphate doped by nickel oxide nanoparticles for capacitive adsorption of reactive red 141 azo dye. Environ Res 184:109322

Hassanzadeh-Tabrizi S, Motlagh MM, Salahshour S (2016) Synthesis of ZnO/CuO nanocomposite immobilized on $\gamma$-$Al_2O_3$ and application for removal of methyl orange. Appl Surf Sci 384:237–243

Ibrahim MM (2019) $Cr_2O_3$/$Al_2O_3$ as adsorbent: Physicochemical properties and adsorption behaviors towards removal of congo red dye from water. J Environ Chem Eng 7(1):102848

Joseph J, Radhakrishnan RC, Johnson JK, Joy SP, Thomas J (2020) Ion-exchange mediated removal of cationic dye-stuffs from water using ammonium phosphomolybdate. Mater Chem Phys 242:122488

Kataria N, Garg V (2019) Application of EDTA modified $Fe_3O_4$/sawdust carbon nanocomposites to ameliorate methylene blue and brilliant green dye laden water. Environ Res 172:43–54

Kumar KV, Sivanesan S (2007) Isotherms for Malachite Green onto rubber wood (Hevea brasiliensis) sawdust: comparison of linear and non-linear methods. Dyes Pigm 72(1):124–129

Lei C, Pi M, Kuang P, Guo Y, Zhang F (2017) Organic dye removal from aqueous solutions by hierarchical calcined Ni-Fe layered double hydroxide: isotherm, kinetic and mechanism studies. J Colloid Interface Sci 496:158–166

Liu H, Zhang J, Lu M, Liang L, Zhang H, Wei J (2020) Biosynthesis based membrane filtration coupled with iron nanoparticles reduction process in removal of dyes. Chem Eng J 387:124202

Manjunatha C, Nagabhushana B, Raghu MS, Pratibha S, Dhananjaya N, Narayana A (2019) Perovskite lanthanum aluminate nanoparticles applications in antimicrobial activity, adsorptive removal of Direct Blue 53 dye and fluoride. Mater Sci Eng C 101:674–685

Mazloomi S, Bonyadi Z, Haghighat GA, Nourmoradi H, Soori MM, Eslami F (2021) Removal of methylene blue by *Saccharomyces cerevisiae*: process modelling and optimization. Desalin Water Treat 236:318–325

Melhi S, Algamdi M, Alqadami AA, Khan MA, Alosaimi EH (2022) Fabrication of magnetically recyclable nanocomposite as an effective adsorbent for the removal of malachite green from water. Chem Eng Res Des 177:843–854

Moghaddam SS, Moghaddam MA, Arami M (2010) Coagulation/flocculation process for dye removal using sludge from water treatment plant: optimization through response surface methodology. J Hazard Mater 175(1–3):651–657

Mohammadi A, Daemi H, Barikani M (2014) Fast removal of malachite green dye using novel superparamagnetic sodium alginate-coated $Fe_3O_4$ nanoparticles. Int J Biol Macromol 69:447–455

Mohammed AA, Kareem SL (2019) Adsorption of tetracycline fom wastewater by using Pistachio shell coated with ZnO nanoparticles: equilibrium, kinetic and isotherm studies. Alex Eng J 58(3):917–928

Mohebbrad B, Bonyadi Z, Dehghan AA, Rahmat MH (2019) Arsenic removal from aqueous solutions using *Saccharomyces cerevisiae*: kinetic and equilibrium study. Environ Prog Sustain Energy 38:S398–S402

Nasoudari E, Ameri M, Shams M, Ghavami V, Bonyadi Z2021 The biosorption of Alizarin Red S by *Spirulina platensis*; process modelling, optimisation, kinetic and isotherm studies. Int J Environ Anal Chem. 1–15.

Nath J, Ray L (2015) Biosorption of Malachite green from aqueous solution by dry cells of *Bacillus cereus* M116 (MTCC 5521). J Environ Chem Eng 3(1):386–394

Navaeia A, Yazdani M, Alidadi H, Dankoob M, Bonyadi Z, Dehghan A, Hosseini A (2019) Biosorption of reactive red 120 dye from aqueous solution using *Saccharomyces cerevisiae*: RSM analysis, isotherms, and kinetic studies. Desalin Water Treat 171:418–427

Neha G, Kushwaha AK, Chattopadhyaya M (2011) Kinetics and thermodynamics of malachite green adsorption on banana pseudostem fibers. J Chem Pharm Res 3(1):284–296

Osagie C, Othmani A, Ghosh S, Malloum A, Esfahani ZK, Ahmadi S (2021) Dyes adsorption from aqueous media through the nanotechnology: a review. J Mater Res Technol 14:2195–2218

Pashaei-Fakhri S, Peighambardoust SJ, Foroutan R, Arsalani N, Ramavandi B (2021) Crystal violet dye sorption over acrylamide/graphene oxide bonded sodium alginate nanocomposite hydrogel. Chemosphere 270:129419

Ramavandi B, Farjadfard S, Ardjmand M (2014) Mitigation of orange II dye from simulated and actual wastewater using bimetallic chitosan particles: continuous flow fixed-bed reactor. J Environ Chem Eng 2(3):1776–1784

Ramavandi B, Najafpoor AA, Alidadi H, Bonyadi Z (2019) Alizarin red-S removal from aqueous solutions using *Saccharomyces cerevisia*e: kinetic and equilibrium study. Desalin Water Treat 144:286–291

Rangabhashiyam S, Lata S, Balasubramanian P (2018) Biosorption characteristics of methylene blue and malachite green from simulated wastewater onto *Carica papaya* wood biosorbent. Surf Interfaces 10:197–215

Rodrigues FK, Salau NPG, Dotto GL (2019) New insights about reactive red 141 adsorption onto multi-walled carbon nanotubes using statistical physics coupled with Van der Waals equation. Sep Purif Technol 224:290–294

Santhi T, Manonmani S, Vasantha V, Chang Y (2016) A new alternative adsorbent for the removal of cationic dyes from aqueous solution. Arab J Chem 9:S466–S474

Shabbir S, Faheem M, Ali N, Kerr PG, Wu Y (2017) Periphyton biofilms: a novel and natural biological system for the effective removal of sulphonated azo dye methyl orange by synergistic mechanism. Chemosphere 167:236–246

Veloso CH, Filippov LO, Filippova IV, Ouvrard S, Araujo AC (2020) Adsorption of polymers onto iron oxides: equilibrium isotherms. J Mater Res Technol 9(1):779–788

Wu X-L, Shi Y, Zhong S, Lin H, Chen J-R (2016) Facile synthesis of $Fe_3O_4$-graphene@ mesoporous $SiO_2$ nanocomposites for efficient removal of methylene Blue. Appl Surf Sci 378:80–86

Zhang L, Huang T, Zhang M, Guo X, Yuan Z (2008) Studies on the capability and behavior of adsorption of thallium on nano-$Al_2O_3$. J Hazard Mater 157(2–3):352–357